JACS
JOURNAL OF THE AMERICAN CHEMICAL SOCIETY

Helically Chiral Hybrid Cyclodextrin Metal-Organic Framework with Circularly Polarized Luminescence

Masoud Kazem-Rostami, [§] Angel Orte, [+] Ana M. Ortuño, [¥] Arthur H. G. David, [§] Indranil Roy, [§] Delia Miguel, [+] Amine Garci, [§] Carlos M. Cruz, [¥] Charlotte L. Stern, [§] Juan M. Cuerva, [¥]* J. Fraser Stoddart *,[§,#,‡,£]

§ Department of Chemistry, Northwestern University, 2145 Sheridan Road, Evanston, Illinois 60208-3133, United States
+ Nanoscopy-UGR Laboratory, Departamento de Fisicoquimica, Facultad de Farmacia, Unidad de Excelencia de Química, University of Granada, Granada 18071, Spain
¥ Department of Organic Chemistry, Unidad de Excelencia de Química, University of Granada, Avda. Fuentenueva, Granada 18071, Spain
 # School of Chemistry, University of New South Wales, Sydney, NSW 2052, Australia
‡ Stoddart Institute of Molecular Science, Department of Chemistry, Zhejiang University, Hangzhou 310021, China
£ ZJU-Hangzhou Global Scientific and Technological Innovation Center, Hangzhou 311215, China

*E-mail: jmcuerva@ugr.es , stoddart@northwestern.edu

MAIN TEXT

*Correspondence Address	*Correspondence Address
Professor Juan M Cuerva Department of Organic Chemistry Unidad de Excelencia de Química University of Granada Granada, 18071 (Spain) Tel: (+34)-958-243-319 E-Mail: *jmcuerva@ugr.es*	Professor J Fraser Stoddart Department of Chemistry Northwestern University 2145 Sheridan Road Evanston, IL 60208-3113 (USA) Tel: (+1)-847-491-3793 E-Mail: *stoddart@northwestern.edu*

ABSTRACT

Three achiral polycyclic aromatic fluorophores—namely, 1-pyrenecarboxylic acid, 9-anthracenecarboxylic acid, and perylene-3,9-dicarboxylic acid—were chosen based on their desired properties before being incorporated into the construction of a K^+-carrying gamma-cyclodextrin-based metal-organic framework (CD-MOF-1) and γ-cyclodextrin (γ-CD) containing hybrid frameworks (CD-HFs). Among these fluorophores, only the pyrene-carrying one shows significant noncovalent bonding interactions (NCIs) with γ-CD in solution. This fluorophore is encapsulated in a CD-HF with a trigonal superstructure instead of the common cubic CD-MOF-1 found in the case of the other two fluorophores. Single-crystal X-ray diffraction analysis of the trigonal CD-HF reveals a π-stacked chiral positioning of the pyrene-carrying fluorophore inside the $(\gamma\text{-CD})_2$ tunnels and held uniformly around an enantiomorphous 3_2 screw axis along the *c* direction in the solid-state structure. This helix-like structure demonstrates an additional level of chirality over and above the point-chiral stereogenic centers of γ-CD and the axial chirality associated with the self-assembled π-stacked fluorophores. These arrangements result in specifically generated photophysical and chiroptical properties, such as controlled emergence of circularly polarized luminescence (CPL) emission. In this manner, a complete understanding of the mechanism of chirality transfer from a chiral host (CD-HF) to an encapsulated achiral fluorophore has been achieved, an attribute which is often missing in the development of materials with CPL.

INTRODUCTION

Cyclodextrin-based metal-organic frameworks[1] (CD-MOFs) constitute a class of porous, renewable, green, and edible metal-organic frameworks (MOFs) derived from γ-cyclodextrin (γ-CD) and alkali metal cations. CD-MOFs are comprised (Figure 1) of extended body-centered frameworks containing $(\gamma\text{-CD})_6$ cubes interconnected by cations, cylindrical $(\gamma\text{-CD})_2$ tunnels and triangular channels between spherical pores of diameter 1.7 nm. As a result, the extended porous structure of CD-MOFs can host a wide variety of guest molecules including gases, drugs, metal-based nanoclusters, and nanoparticles. CD-MOFs offer potential applications in areas as disparate as the templated synthesis of metal-based nanoparticles and gels,[2] the reversible absorption of gases,[3] high-performance separations,[4] regio- and enantioselective reactions,[5] the trapping and investigation of highly reactive intermediates,[6] catalysis,[7] electrochemical sensing,[8] information storage in memristors,[9] drug delivery systems,[10] and, most recently, in chiroptical materials.[11]

Circularly polarized luminescence (CPL) emission is the difference of emission between left- and right-handed circularly polarized light emitted by chiral fluorophores.[12] This phenomenon can be detected in small organic molecules,[13] organometallic complexes,[14] and supramolecular assemblies.[15] Recently, the investigation[16] of CPL emission has been on the increase, especially in relation to MOFs.[17] CPL Emission is a unique photophysical property that offers applications in the design of sensors,[18] circularly polarized organic light-emitting diodes, [19] CP-lasers,[20] and security inks.[21] In this context, the investigation of the chiroptical properties in MOFs opens up a new chapter in the design and performance of smart materials featuring CPL emission where these chiroptical properties and the exceptional characteristics of MOFs, *e.g.* ordered nanoporosity, are combined.

Since CD-MOFs are positively charged, their voids naturally host hydroxide or chloride anions associated with their alkali metal cations in order to balance the overall charge and maintain neutrality.[1a] Although the metal cations are located in the CD-MOFs' lattice structure, the anions remain mobile and can be exchanged with anionic guests. Furthermore, the cubic voids in CD-MOFs encompass the point chirality of γ-CD, creating chiral environments that enable the transfer of chirality to achiral guests. Capitalizing on the intrinsic stereogenic centers of γ-CD, Liu and co-workers[11] incorporated 12 achiral fluorophores into CD-MOFs. They found that the crystallinity of these MOFs boost the CPL dissymmetry factor (g_{lum}) in comparison with the emission of blended amorphous powders. In addition, they concluded that a strong negative CPL emission is induced when the size of guest fluorophores matches the voids, while smaller fluorophores lead to random and uncontrolled CPL emissions. Although this pioneering study deserves the credit it has earned[11], some important aspects have been left unexplored. One of them is the exact origin of the chirality transfer from the chiral host to achiral guests. Understanding this transfer of chirality at a molecular level is indispensable for the development of more efficient CPL emitters.

In this context, we chose three achiral fluorophores—namely,[22] 1-pyrenecarboxylic acid (PyCA), 9-anthracenecarboxylic acid (AnCA), and perylene-3,9-dicarboxylic acid (PeCA)—based on their size, geometry, availability, ionization mode, stability, and solubility. Here, we report our investigation of their noncovalent bonding interactions (NCIs) with γ-CD and determine their binding constants in aqueous alkaline solutions. This basic medium mimics the mother liquor in which CD-MOF crystals grow (Figure 2). Next, we incorporated these fluorophores in the construction of CD-MOFs so that we can visualize their solid-state superstructures by single-crystal X-ray diffraction and report first-hand the helix-like chiral positioning of PyC^- dimers in CD-HF. We also performed ^{1}H NMR spectroscopic analyses of the digested CD-MOFs in order

to quantify the ratio of the fluorescent guests to γ-CD in the CD-MOFs, which had been pre-loaded with the fluorophores by diffusion and during co-crystallization. Finally, we present a detailed study of the crystal structure of PyC^{-}⊂CD-HF, where PyC^{-} is the carboxylate, displaying precisely how the π-stacked dimers of this achiral emitter reside in the $(\gamma\text{-CD})_2$ tunnels and establish clear-cut hydrogen bonding interactions between the carboxylate and hydroxyl groups on the secondary (2°) face of the $(\gamma\text{-CD})_2$ tunnels in PyC^{-}⊂CD-HF. Our investigations also reveal how PyC^{-}⊂γ-CD units in the CD-HF are oriented around an enantiomorphous 3_2 screw axis in an axially chiral solid-state structure. This arrangement results in the generation of a static excimer-based CPL emission,[23] which is one of the most promising approaches for achieving an intense CPL emission.[24] In addition, we elaborate on the geometrical structural factors and changes in the symmetry of the solid-state superstructures. The understanding of these superstructural factors facilitates the achievement of controlled CPL emissions.

RESULTS AND DISCUSSION

The CD-MOF original recipe starts from an aqueous alkali metal solution with γ-CD whose subjection to vapor diffusion of MeOH, EtOH, or Me_2CO yields the metal-organic framework in the form of transparent cubic crystals. The addition of compatible solutes to crystallization medium, capable of penetrating[1b] the MOF, results in the formation of CD-MOFs loaded[1a] with the solutes. We exploited this method to obtain CD-MOFs hosting three fluorophores, namely PyCA, AnCA, and PeCA. These fluorophores are small enough for inclusion inside the $(\gamma\text{-CD})_2$ tunnels of CD-MOFs, and they remain there in the form of negatively charged conjugate carboxylates, making them both soluble in the basic aqueous media required for CD-MOF synthesis and desirable for the subsequent anion exchange.[5,25] The ^{1}H NMR spectroscopic analysis after digestion of these CD-MOFs with D_2O revealed[26] the relative ratios of AnC^{-}, PyC^{-}, PeC^{-} to γ-CD as 2.10:1, 0.82:1,

and 0.37:1, respectively. See Figures S1–S3 and Table S1 in the Supporting Information (SI). Another approach for the inclusion of small molecules in CD-MOFs is to first of all prepare the crystalline MOF and then immerse it in an organic solution containing a negatively charged guest (or guests) in order to replace the hydroxide or chloride anions by diffusion.[10b,27] The diffusion method, at its best, resulted in a relative ratio (Table S1) of 0.98:1 for AnC^- to γ-CD based on ^1H NMR spectroscopy (Figure S4) following digestion, while showing no AnC^- guests in the crystal structure obtained by X-ray diffraction. Use of the diffusion method did not alter the structure of the cubic CD-MOF-1, whose details will be discussed later.

Following the digestion procedures and ^1H NMR analyses revealing significant quantities of guests included in the CD-MOFs, we were encouraged to examine the fluorophore-loaded CD-MOFs by single-crystal X-ray diffraction. The results of X-ray crystallographic diffraction, however, did not display any guests when the CD-MOFs constituted (Figure 1) the common *I*432 cubic unit cell with approximate dimensions of 31 × 31 × 31 Å ($\alpha = \beta = \gamma = 90°$). The most intense Q-peak (1.8–1.9 residual electron density, among 75 others) present in the difference map of the cubic unit cell in Olex2[28] was not associated with any other entities and hence was assigned to disordered H_2O molecules. This observation attests to the random and directionless positioning of the guests whose presence could not be detected by X-ray diffraction, on account of destructive interference of the randomly placed molecules since constructive interference which only detects repeating patterns across extended domains. Nonetheless, serendipitously, when $PyC^-\subset$CD-HF was allowed to form by co-crystallization, the crystal structure assumed a new chiral space group, $P3_221$, with unit cell dimensions of 43.1 × 43.1 × 56.0 Å ($\alpha = \beta = 90°$, $\gamma = 120°$), representing (Figure 2a–c) the $(\gamma\text{-CD})_2$ tunnels hosting two π-stacked PyC^- guests. See the Supporting Information (SI) for more details. The aromatic planes of these π-stacked PyC^- anions subtend an angle of 3.7° and relative rotation

of 10.4° (Figure S17), with an approximate average distance of 4 Å between the planes (Figure 2b), thus breaking centrosymmetry and resulting in a chiral dimeric structure. The unidirectional staggered π-stacking of PyC^- anions—along with the hydrogen-bonding interactions associated with their carboxylate groups and the C2-OH and C3-OH on the secondary (2°) face[1a] of α-D-glucopyranosyl residues residing inside the $(\gamma\text{-CD})_2$ tunnels (Figure 3) in the CD-HF—play a significant role in their orientation in the crystal and their detection (Figures 2, 3, and S11–S16) by X-ray diffraction. This phenomenon can be explained by the binding affinity of PyC^- with γ-CD. According to the data obtained by ^{1}H NMR spectroscopic titrations (See Figures S5–S10), the binding constant of PyC^- to γ-CD is 62.0 ± 1.0 M^{-1} (see Table S3), while those found for AnC^-, and PeC^- are negligible. Taking the oxygen atoms of the inward-facing secondary OH groups of the α-D-glucopyranosyl residues as contact points, X-ray diffraction reveals that the crisscrossed distances of CH-OH(γ-CD torus 1) to its opposing counterpart CH-OH(γ-CD torus 2) change dramatically, revealing that a new set of NCIs is introduced by inclusion of a pair of PyC^- anions. Figures 3a and 3b show that the crisscrossed spatial distances of [C2-OH(γ-CD torus 1) – C2-OH(γ-CD torus 2)] and [C3-OH(γ-CD torus 1) – C3-OH(γ-CD torus 2)] are ca. 5.2 and 4.6 Å, respectively, where the CH-OH groups are free. These distances are equal at about 5.3 Å when the CH-OH groups coordinate with a K^+-ion in the cubic CD-MOF-1 system (Figures 1 and 3a–b). The X-ray diffraction, resulting from the helical chiral CD-HF system (Figures 3c–f), reveals that the inclusion of PyC^- anions inside $(\gamma\text{-CD})_2$ tunnels in the CD-HF causes the distances for [C2-OH(γ-CD torus 1) – C2-OH(γ-CD torus 2)] and [C3-OH(γ-CD torus 1) – C3-OH(γ-CD torus 2)] to be slightly different. Thus, these distances are about 4.8–4.9 and 5.3–5.6 Å in the absence—and about 4.8–5.3 Å in the presence—of K^+ cation coordination to the side of the tori when the C-OH groups also interact with the carboxylate groups on the PyC^- anions. These interactions consist of

multiple hydrogen bonds that pull (Figures 3c–f) the two γ-CD rings in CD-HF slightly closer to one another when the positive charge of the metal cation is countered with the negative charge of the carboxylate. Since X-ray diffraction cannot pinpoint hydrogen atoms, our argument regarding the balancing charges here is based on the high pHs at which the CD-MOFs were grown. See Section A of the SI. In contrast, at the other side of the $(\gamma\text{-CD})_2$ tunnels hosting the hydrophobic bulk of the nonpolar aromatic moiety of the PyC^- anion, these distances become (Figures 3c–f) as large as 6.4 and 7.3 Å at the nearest—and at about 7.4 and 7.5 Å at the furthest—edges of the aromatic plane from the carboxylate group. We also noticed that the diagonal spatial distance between the glycocidic oxygen atoms of α-D-glucopyranosyl residues residing in $(\gamma\text{-CD})_2$ tunnels of the CD-MOF-1 are almost always equal at 13.4–13.8 Å (*i.e.*, nearly circular) in the cubic CD-MOF-1, while they show a broader range of 12.5–14.1 Å (*i.e.*, slightly oval) in the trigonal $PyC^-\subset$CD-HF. Therefore, the inclusion of PyC^- anion and its NCIs with γ-CDs in the CD-HF cause (Figure 4a–c) geometrical changes in the tori that influence the assembly of these building blocks, leading to the formation of a trigonal CD-HF with a helically chiral superstructure.

We also analyzed the CD-MOFs by powder X-ray diffraction (Figure 4d), fluorescence confocal microscopy, and scanning electron microscopy (SEM) in order to screen the homogeneity of the CD-MOF samples in bulk. See Sections C and D of the SI. Powder X-ray diffraction analyses showed that, despite the same symmetry of pristine CD-MOF-1, cubic $AnC^-\subset$CD-MOF-1, and $PeC^-\subset$CD-MOF-1, the latter two noticeably lack a peak at 8.0° and show (Figure 4d) a much lower intensity at 5.7°. This observation might result from the suppression of diffractions at particular angles by re-diffraction and absorption occurring in the presence of the fluorophores in the $(\gamma\text{-CD})_2$ tunnels (Figure S18). In contrast, $PyC^-\subset$CD-HF, whose trigonal structure assumes a new chiral space group ($P3_221$) displayed (Figure 4d) a different powder X-ray diffraction pattern

compared to those recorded for the cubic CD-MOFs. This diffraction pattern corresponded (Figure S20) to the simulated data obtained for a previously reported[1a] trigonal CD-HF. The trigonal CD-HF hosting π-stacked PyC^- anions, however, presents an elongated unit cell along the *c* direction in order to accommodate the helix-like positioning of PyC^- anions around an enantiomorphous 3_2 screw axis. Therefore PyC^-⊂CD-HF assumed the $P3_221$ chiral space group with a cell volume of 90,233 $Å^3$ and a cell dimension of 56 Å along the *c* direction *i.e.* twice as large as our previously reported[1a] trigonal CD-HF that assumed the *R*32 space group, whose cell volume and dimension along the *c* direction were 44,843 $Å^3$ and 28 Å, respectively.

Next, we investigated the induced chirality and its relation to the photophysical properties of PyC^- anions in PyC^-⊂CD-HF using a combination of steady-state and time-resolved fluorescence microscopy and CPL spectroscopy. PyC^-⊂CD-HF crystals exhibit striking photophysical properties, such as a quantum yield of 38 ± 1% in the solid-state. See Section E of the SI for details. The crystal also exhibit (Figures 5b and 5d) a long average luminescence lifetime, τ, of 45.3 ± 4.2 ns over a broad emission band centered at 480 nm that resembles pyrenes' excimer emission. See Sections D–F of the SI for more details. Individual crystals analyzed (Figure 5b and S27b) by FLIM imaging showed (Figure 5a and 5c) analogous emission spectra within different areas of the crystals. The kinetics of the emission from individual PyC^-⊂CD-HF crystals in FLIM images were fitted to a bi-exponential decay function, exhibiting two decay components—the major component centered (Figure 5d and S27) at around 40 ns and a less abundant contribution at 16 ns. Since in the crystal form the PyC^- anions have no mobility, this excimer-type emission band must arise from the pre-associated static excimer. This behavior is proven unequivocally by the fact that both emitting components from the time-resolved emission-decay traces and FLIM images present

positive pre-exponential factors, represented by only positive populations in their lifetime distributions, thus eliminating the possibility of dynamic processes in the excited state[22a].

In order to investigate the CPL emission of $PyC^{-}\subset$CD-HF, we focused on the dimensionless luminescence dissymmetry ratio g_{lum}, defined as $g_{lum} = 2(I_L-I_R)/(I_L+I_R)$, where I_L and I_R are, respectively, the intensities of the emitted left and right circularly polarized light. This parameter provides a quantitative estimation of circularly polarized emitted radiation over the total emitted radiation. It is worth noting that g_{lum} usually collects the information about an isotropic distribution of chiral emitters lacking in any macroscopic anisotropy or photoselection artifacts[29]. Therefore, reliable measurement of isotropic g_{lum} ratios in solid, especially crystalline, samples is complex. As a result, despite the stunning photophysical properties of $PyC^{-}\subset$CD-HF crystals, we decided to use a suspension of the solid material in MeOH, thus avoiding any highly oriented macroscopic anisotropy in the material. The sample was also ground until a constant and reliable signal for $g_{lum} = +3.5\times10^{-3}$ was obtained (Figure 6a), is stronger than those reported by Takashima *et al.*[30] ($g_{lum} =2.2\times10^{-3}$) reported for pyrene containing γ-CDs, and the $PyC^{-}\subset$CD-MOF that Liu and co-workers[11] ($g_{lum} =1\times10^{-3}$) described. In addition, this value is in the same range as two examples also described by the same authors[11] presenting tetraphenylethylene-based tetracarboxylate ligands or Ru(III)bipyridine complexes encapsulated in CD-MOFs ($g_{lum} =2\times10^{-3}$, 8×10^{-3} respectively). Importantly, the contribution of photoselection to the g_{lum} value under this experimental setup was ruled out using Dekkers' procedure[31]. This artifact-free condition is perhaps facilitated by the optimal reorientation of the solid emitter in the stirred suspension, prior to observation of the emission, as allowed by the long luminescence lifetime. Because the experiment made use of a suspension of the material, some leaking of monomeric PyC^{-} anions is inevitable, as evidenced by the coexistence of both monomeric (< 400 nm) and excimer-type (ca.

500 nm) emission bands (Figure 6b, green trace). In order to shed light on the nature of these bands, we performed time-resolved emission spectroscopy (TRES) and FLIM imaging experiments on a suspension of $PyC^{-}\subset$CD-HF crystals in MeOH. TRES deconvolution of the emission spectra—see Figure S26 and read SI for details of the analysis—showed (Figure 6b) three different species with lifetimes of 2, 12 and 42 ns. These are the so-called species-associated emission spectra (SAEMS). FLIM images of individual crystals in MeOH (Figures 6c–e and Figure S28) exhibit a bathochromic shift and longer average luminescence lifetimes than did the dried crystals. Some dynamic contributions, which we attribute to negative pre-exponential factors, were detected in the pyrene excimer-emission region. These contributions probably correlated with the minimal mobility of both PyC^{-} anions inside the $(CD)_2$ tunnels in the presence of MeOH. This dynamic is clearly visible in the TRES analysis, where the spectrum associated with the 12-ns emitter has a negative pre-exponential with a minimum centered around 500 nm (Figure 6b, red dots). Likewise, luminescence-lifetime distributions of the FLIM images showed (Figure 6e and S28b) a negative population, broadly distributed and peaking at around 6 ns with an average value of 7.9 ns. The presence of such contributions is related to the existence of dynamic PyC^{-}–PyC^{-} interactions within the time frame of the excited state. The detection of localized dynamic excimers in FLIM imaging has been accounted[32] for only recently and constitutes a novel image-filtering tool called DYNEX. Applying the DYNEX criterion to images of $PyC^{-}\subset$CD-HF in MeOH reveals (Figure S28c) the specific points where actual dynamic excimer formation is detected. All these effects result globally in an increased bathochromic shift and longer average luminescence lifetimes than those of the dried crystals (Figure S27). It is worth noting that the only CPL-active band is that centered at the emission of PyC^{-} excimers (Figure 6a), thus confirming the notion that no macroscopic artifacts affecting the global emission are present, and that CPL emission arises from

the $PyC^{-}\subset$CD-HF, where the PyC^{-} anions are in close proximity. We reasoned that the observed CPL emission at 500 nm must result from a combination of contributions of static excimer and dynamic interactions inside the $(\gamma\text{-CD})_2$ tunnels. Our results confirm that chirality has been transferred from the CD-HF extended structure to a static as well as a dynamic excimer of PyC^{-} with in-void mobility in the presence of MeOH. Although the corresponding enantiomer of the CD-HF is not available for investigation, we can also confirm the reliability of the signal based on Mori's finding,[33] which indicates that in rigid systems the CPL signal coming from the $S_1 \rightarrow S_0$ transition is of the same sign and magnitude as that of the $S_0 \rightarrow S_1$ transition. To this end, both the $S_0 \rightarrow S_1$ and $S_1 \rightarrow S_0$ transitions were simulated computationally. See SI for details. Taking into account the complexity of the system, the geometry of the two PyC^{-} anions present in the $(\gamma\text{-CD})_2$ tunnels was directly taken from the X-ray diffraction structure. The geometry optimization of the S_1 excited state of the γCD–PyC^{-}–PyC^{-} complex is required to calculate the electric and magnetic transition dipole moments of the $S_1 \rightarrow S_0$ transition.[30] Optimization of the S_1 excited state for this supramolecular system, using a reliable density functional and basis set, would demand a tremendous amount of computational time. Additionally, the direct optimization of the S_1 excited state of the two PyC^{-} anions, in the absence of the γ-CD torus, afforded geometries that did not match the available cavity space. Therefore, the coordinates of the carboxylate as well as the opposite aromatic carbon of each PyC^{-} anion were frozen to simulate the $(\gamma\text{-CD})_2$ tunnels in the CD-HF, and the geometry of the S_1 excited state was then optimized. From the modules of the electric transition dipole moment, and magnetic transition dipole moment, the calculated g_{lum} value of the $S_1 \rightarrow S_0$ transition was estimated as +0.0022, a value similar in sign and order of magnitude to the experimental one (+0.0035), and also in accord with the calculated g_{abs} value (+0.0023).

■ CONCLUSION

Our findings, which are in agreement with our earlier discoveries[1b], suggest that the absence of NCIs between the fluorophores and γ-CD does not necessarily diminish the capacity of CD-MOF-1 toward the encapsulation of the fluorophores. It may lead, however, to a random and disordered harboring of the fluorophores in the tunnels and voids of cubic CD-MOF-1. This disoriented positioning of fluorophores and their lack of specific order prevent their uniform assembly and visualization by single-crystal X-ray diffraction and, consequently, lead to loss of control over the transfer of chirality. This situation may result in randomized and unpredictable CPL emission values having both positive and negative signs, as Liu and co-authors[11] have observed for small fluorophores. Based on the experimental data and the accumulated knowledge in the literature, it can be suggested that the co-crystallization of γ-CD with solutes lacking NCIs most often leads to the cubic CD-MOF-1. This behavior is similar to the diffusion methods that naturally do not change the CD-MOF-1's original cubic structures despite allowing the inclusion of solutes into them. Among the three achiral fluorophores we investigated for incorporation into CD-MOFs, only PyC^- anions featured considerable NCIs with γ-CD in solution. These NCIs lead to the generation of a fluorophore-loaded CD-HF characterized by a helix-like chiral superstructure while the two other fluorophores co-crystallized with γ-CD in the common cubic form of CD-MOF-1.

We have demonstrated previously[5] that some similar polycyclic aromatic dyes fail to π-stack on their own in the solid-state, despite the extensive aromatic planes they possess. Nonetheless, their incorporation in the CD-HF secured their positioning in specific ways as a consequence of their NCIs with γ-CD. This work reveals that NCIs effectively influence the $(\gamma\text{-CD})_2$ tunnels by holding the π-stacked PyC^- fluorophores uniformly with a controlled axial chirality. These NCIs act in

concert with the anion-exchange mechanism to rearrange the building blocks, preassembling them in a specific way toward the formation of a chiral unit cell whose growth results in the extended structure of a helix-like chiral CD-HF. The inclusion of the achiral PyC^- fluorophore in the point-chiral γ-CD's tori in the CD-HF led to a transfer of chirality from the tori to the π-stacked fluorophores, which themselves became axially chiral. In addition to this phenomenon, the helix-like solid-state extended structure of the CD-HF added another level of chirality by holding the π-stacked PyC^- anionic dimers around an enantiomorphous 3_2 screw axis, further boosting the chirality effects on PyC^- in the CD-HF. We have visualized the detailed structure of this helix-like chiral CD-HF by single-crystal X-ray diffraction and investigated its photophysical and correlated chiroptical properties. Our findings have led to a deeper understanding of the origin of the chirality transfer for small fluorophores in crystalline CD-HF by a controlled angle between the subunits of the stacked π-systems. This observation was particularly interesting, as g_{lum} values are highly dependent on such angles. Our results pave the way for the development of a smart combination of chiral hosts and excimer-like emissions with other angle distributions. We can confirm that this solid-state superstructure has a controlled and predictable excimer-like CPL emission from an achiral fluorophore encapsulated in a chiral CD-HF. We anticipate that additional fluorophores capable of NCIs could be used for the rational construction of hybrid CD-MOFs with predictable CPL controlling the geometric parameters in the chiral unit cell. This research elaborates on the structural factors and changes in the symmetry of the solid-state superstructures that result in a controlled emergence of CPL emissions. In this way, a complete understanding of the mechanism of chirality transfer from a chiral host to an encapsulated achiral fluorophore has been achieved, a finding that furthers the development of materials with CPL emission.

■ ASSOCIATED CONTENT

Supporting Information

Detailed procedures and characterization data are available free of charge via the internet at http://pubs.acs.org. CCDC-2091539, CCDC-2121336 and CCDC-2121337 contain crystallographic data for this work which can be obtained free of charge via www.ccdc.cam.ac.uk (or from the Cambridge Crystallographic Data Center, 12, Union Road, Cambridge CB2 1EZ, UK; fax: +441223 336033).

■ AUTHOR INFORMATION

Corresponding Author

*E-mail: jmcuerva@ugr.es, stoddart@northwestern.edu

Notes

The authors declare no competing financial interests.

■ ACKNOWLEDGMENTS

The authors thank both Northwestern University (NU) and the University of Granada (UGR) for their continued support of this research. NU authors acknowledge the Integrated Molecular Structure Education and Research Center (IMSERC) for providing access to equipment for the experiments. This research made use of the NUFAB facility of NUANCE Center and Biological Imaging Facility (RRID:SCR_017767) supported by the Chemistry for Life Processes Institute at NU, the supercomputing facilities of the Service and Support for Science IT (S^3IT) of the University of Zurich (UZH), and the CSIRC computational facilities at UGR. The NUANCE Center has received support from the SHyNE Resource (NSF ECCS-2025633), the IIN, and Northwestern's MRSEC program (NSF DMR-1720139). This research was also supported by

FEDER/Junta de Andalucía-Consejería de Economía y Conocimiento/ Proyecto P20_00162 and projects PID2020-113059GB-C21 and PID2020-114256RB-I00 funded by MCIN/AEI/10.13039/501100011033 in Spain. Ana M. Ortuño acknowledges her FPU contract (FPU16/02597) funded by MCIN/AIE/10.13039/501100011033 and FSE "El FSE invierte en tu futuro" Spain. Carlos M. Cruz acknowledges with thanks Prof. Dr. Michal Juríček for his support and access to computing facilities. Associate Professor Christos D. Malliakas (IMSERC's Crystallography Director), and Dr. Jessica E. Hornick (Operations Director of Northwestern University Biological Imaging Core Facility) are thanked especially for their invaluable assistance throughout this project.

■ REFERENCES

(1) (a) Smaldone, R. A.; Forgan, R. S.; Furukawa, H.; Gassensmith, J. J.; Slawin, A. M. Z.; Yaghi, O. M.; Stoddart, J. F., Metal–Organic Frameworks from Edible Natural Products. *Angew. Chem. Int. Ed.* **2010**, *49*, 8630–8634. (b) Roy, I.; Stoddart, J. F., Cyclodextrin Metal–Organic Frameworks and Their Applications. *Acc. Chem. Res.* **2021**, *54*, 1440–1453.

(2) Wei, Y.; Han, S.; Walker, D. A.; Fuller, P. E.; Grzybowski, B. A., Nanoparticle Core/Shell Architectures within MOF Crystals Synthesized by Reaction Diffusion. *Angew. Chem. Int. Ed.* **2012**, *51*, 7435–7439.

(3) (a) Gassensmith, J. J.; Furukawa, H.; Smaldone, R. A.; Forgan, R. S.; Botros, Y. Y.; Yaghi, O. M.; Stoddart, J. F., Strong and Reversible Binding of Carbon Dioxide in a Green Metal–Organic Framework. *J. Am. Chem. Soc.* **2011**, *133*, 15312–15315. (b) Patel, H. A.; Islamoglu, T.; Liu, Z.; Nalluri, S. K. M.; Samanta, A.; Anamimoghadam, O.; Malliakas, C. D.; Farha, O. K.; Stoddart, J. F., Noninvasive Substitution of K^+ Sites in Cyclodextrin Metal–Organic Frameworks by Li^+ Ions. *J. Am. Chem. Soc.* **2017**, *139*, 11020–11023.

(4) (a) Hartlieb, K. J.; Holcroft, J. M.; Moghadam, P. Z.; Vermeulen, N. A.; Algaradah, M. M.; Nassar, M. S.; Botros, Y. Y.; Snurr, R. Q.; Stoddart, J. F., CD-MOF: A Versatile Separation Medium. *J. Am. Chem. Soc.* **2016**, *138*, 2292–2301. (b) Holcroft, J. M.; Hartlieb, K. J.; Moghadam,

P. Z.; Bell, J. G.; Barin, G.; Ferris, D. P.; Bloch, E. D.; Algaradah, M. M.; Nassar, M. S.; Botros, Y. Y.; Thomas, K. M.; Long, J. R.; Snurr, R. Q.; Stoddart, J. F., Carbohydrate-Mediated Purification of Petrochemicals. *J. Am. Chem. Soc.* **2015**, *137*, 5706–5719.

(5) Chen, X.-Y.; Chen, H.; Đorđević, L.; Guo, Q.-H.; Wu, H.; Wang, Y.; Zhang, L.; Jiao, Y.; Cai, K.; Chen, H.; Stern, C. L.; Stupp, S. I.; Snurr, R. Q.; Shen, D.; Stoddart, J. F., Selective Photodimerization in a Cyclodextrin Metal–Organic Framework. *J. Am. Chem. Soc.* **2021**, *143*, 9129–9139.

(6) Nuñez-Lopez, A.; Galbiati, M.; Padial, N. M.; Ganivet, C. R.; Tatay, S.; Pardo, E.; Armentano, D.; Martí-Gastaldo, C., Direct Visualization of Pyrrole Reactivity Upon Confinement within a Cyclodextrin Metal–Organic Framework. *Angew. Chem. Int. Ed.* **2019**, *58*, 9179–9183.

(7) (a) Han, S.; Wei, Y.; Grzybowski, B. A., A Metal–Organic Framework Stabilizes an Occluded Photocatalyst. *Chem. Eur. J.* **2013**, *19*, 11194–11198. (b) Zhao, Y.; Zhuang, S.; Liao, L.; Wang, C.; Xia, N.; Gan, Z.; Gu, W.; Li, J.; Deng, H.; Wu, Z., A Dual Purpose Strategy to Endow Gold Nanoclusters with Both Catalysis Activity and Water Solubility. *J. Am. Chem. Soc.* **2020**, *142*, 973–977.

(8) (a) Gassensmith, J. J.; Kim, J. Y.; Holcroft, J. M.; Farha, O. K.; Stoddart, J. F.; Hupp, J. T.; Jeong, N. C., A Metal–Organic Framework-Based Material for Electrochemical Sensing of Carbon Dioxide. *J. Am. Chem. Soc.* **2014**, *136*, 8277–8282. (b) Han, S.; Wei, Y.; Valente, C.; Forgan, R. S.; Gassensmith, J. J.; Smaldone, R. A.; Nakanishi, H.; Coskun, A.; Stoddart, J. F.; Grzybowski, B. A., Imprinting Chemical and Responsive Micropatterns into Metal–Organic Frameworks. *Angew. Chem. Int. Ed.* **2011**, *50*, 276–279.

(9) Yoon, S. M.; Warren, S. C.; Grzybowski, B. A., Storage of Electrical Information in Metal–Organic-Framework Memristors. *Angew. Chem. Int. Ed.* **2014**, *53*, 4437–4441.

(10) (a) Li, H.; Lv, N.; Li, X.; Liu, B.; Feng, J.; Ren, X.; Guo, T.; Chen, D.; Stoddart, J. F.; Gref, R.; Zhang, J., Composite CD-MOF Nanocrystals-Containing Microspheres for Sustained Drug Delivery. *Nanoscale* **2017**, *9*, 7454–7463. (b) Hartlieb, K. J.; Ferris, D. P.; Holcroft, J. M.; Kandela, I.; Stern, C. L.; Nassar, M. S.; Botros, Y. Y.; Stoddart, J. F., Encapsulation of Ibuprofen in CD-MOF and Related Bioavailability Studies. *Mol. Pharmaceutics* **2017**, *14*, 1831–1839.

(11) Hu, L.; Li, K.; Shang, W.; Zhu, X.; Liu, M., Emerging Cubic Chirality in Cyclodextrin-MOF for Fabricating Circularly Polarized Luminescent Crystalline Materials and the Size Effect. *Angew. Chem. Int. Ed.* **2020**, *59*, 4953–4958.

(12) (a) Riehl, J. P.; Richardson, F. S., Circularly Polarized Luminescence Spectroscopy. *Chem. Rev.* **1986**, *86*, 1–16. (b) Longhi, G.; Castiglioni, E.; Koshoubu, J.; Mazzeo, G.; Abbate, S., Circularly Polarized Luminescence: A Review of Experimental and Theoretical Aspects. *Chirality* **2016**, *28*, 696–707.

(13) Mori, T., *Circularly Polarized Luminescence of Isolated Small Organic Molecules. 1st ed.*; Springer Nature, Singapore **2020**.

(14) (a) Wong, H.-Y.; Lo, W.-S.; Yim, K.-H.; Law, G.-L., Chirality and Chiroptics of Lanthanide Molecular and Supramolecular Assemblies. *Chem* **2019**, *5*, 3058–3095. (b) Doistau, B.; Jiménez, J.-R.; Piguet, C., Beyond Chiral Organic (P-Block) Chromophores for Circularly Polarized Luminescence: The Success of D-Block and F-Block Chiral Complexes. *Front. Chem.* **2020**, *8*, 555.

(15) (a) Sang, Y.; Han, J.; Zhao, T.; Duan, P.; Liu, M., Circularly Polarized Luminescence in Nanoassemblies: Generation, Amplification, and Application. *Adv. Mater.* **2020**, *32*, 1900110. (b) David, A. H. G.; Stoddart, J. F., Chiroptical Properties of Mechanically Interlocked Molecules. *Isr. J. Chem.* **2021**, *61*, 608–621. (c) David, A. H. G.; Casares, R.; Cuerva, J. M.; Campaña, A. G.; Blanco, V., A [2]Rotaxane-Based Circularly Polarized Luminescence Switch. *J. Am. Chem. Soc.* **2019**, *141*, 18064–18074.

(16) (a) Shi, Y.; Duan, P.; Huo, S.; Li, Y.; Liu, M., Endowing Perovskite Nanocrystals with Circularly Polarized Luminescence. *Adv. Mater.* **2018**, *30*, 1705011. (b) Zhao, B.; Pan, K.; Deng, J., Intense Circularly Polarized Luminescence Contributed by Helical Chirality of Monosubstituted Polyacetylenes. *Macromolecules* **2018**, *51*, 7104–7111. (c) Di Nuzzo, D.; Cui, L.; Greenfield, J. L.; Zhao, B.; Friend, R. H.; Meskers, S. C. J., Circularly Polarized Photoluminescence from Chiral Perovskite Thin Films at Room Temperature. *ACS Nano* **2020**, *14*, 7610–7616. (d) Niu, D.; Ji, L.; Ouyang, G.; Liu, M., Histidine Proton Shuttle-Initiated Switchable Inversion of Circularly Polarized Luminescence. *ACS Appl. Mater. Interfaces* **2020**, *12*, 18148–

18156. (e) Yang, X.; Jin, X.; Zhao, T.; Duan, P., Circularly Polarized Luminescence in Chiral Nematic Liquid Crystals: Generation and Amplification. *Mater. Chem. Front.* **2021**, *5*, 4821–4832. (f) Wade, J.; Brandt, J. R.; Reger, D.; Zinna, F.; Amsharov, K. Y.; Jux, N.; Andrews, D. L.; Fuchter, M. J., 500-Fold Amplification of Small Molecule Circularly Polarised Luminescence through Circularly Polarised FRET. *Angew. Chem. Int. Ed.* **2021**, *60*, 222–227. (g) Du, S.; Zhu, X.; Zhang, L.; Liu, M., Switchable Circularly Polarized Luminescence in Supramolecular Gels through Photomodulated FRET. *ACS Appl. Mater. Interfaces* **2021**, *13*, 15501–15508.

(17) (a) Qin, T.; Feng, Z.; Yang, J.; Shen, X.; Zhu, D., Unprecedented Three-Dimensional Hydrogen-Bonded Hex Topological Chiral Lanthanide-Organic Frameworks Built from an Achiral Ligand. *Acta Crystallogr., Sect. C* **2018**, *74*, 1403–1412. (b) Chen, S.-M.; Chang, L.-M.; Yang, X.-K.; Luo, T.; Xu, H.; Gu, Z.-G.; Zhang, J., Liquid-Phase Epitaxial Growth of Azapyrene-Based Chiral Metal–Organic Framework Thin Films for Circularly Polarized Luminescence. *ACS Appl. Mater. Interfaces* **2019**, *11*, 31421–31426. (c) Huizi-Rayo, U.; Zabala-Lekuona, A.; Terenzi, A.; Cruz, C. M.; Cuerva, J. M.; Rodríguez-Diéguez, A.; García, J. A.; Seco, J. M.; San Sebastian, E.; Cepeda, J., Influence of Thermally Induced Structural Transformations on the Magnetic and Luminescence Properties of Tartrate-Based Chiral Lanthanide Organic-Frameworks. *J. Mater. Chem. C* **2020**, *8*, 8243–8256. (d) Shang, W.; Zhu, X.; Liang, T.; Du, C.; Hu, L.; Li, T.; Liu, M., Chiral Reticular Self-Assembly of Achiral Aiegen into Optically Pure Metal–Organic Frameworks with Dual Mechano-Switchable Circularly Polarized Luminescence. *Angew. Chem. Int. Ed.* **2020**, *59*, 12811–12816. (e) Zhao, T.; Han, J.; Jin, X.; Zhou, M.; Liu, Y.; Duan, P.; Liu, M., Dual-Mode Induction of Tunable Circularly Polarized Luminescence from Chiral Metal-Organic Frameworks. *Research* **2020**, 6452123. (f) Fu, H.-R.; Wang, N.; Wu, X.-X.; Li, F.-F.; Zhao, Y.; Ma, L.-F.; Du, M., Circularly Polarized Room-Temperature Phosphorescence and Encapsulation Engineering for MOF-Based Fluorescent/Phosphorescent White Light-Emitting Devices. *Adv. Opt. Mater.* **2020**, *8*, 2000330. (g) Zhang, C.; Yan, Z.-P.; Dong, X.-Y.; Han, Z.; Li, S.; Fu, T.; Zhu, Y.-Y.; Zheng, Y.-X.; Niu, Y.-Y.; Zang, S.-Q., Enantiomeric MOF Crystals Using Helical Channels as Palettes with Bright White Circularly Polarized Luminescence. *Adv. Mater.* **2020**, *32*, 2002914. (h) Zeng, M.; Ren, A.; Wu, W.; Zhao, Y.; Zhan, C.; Yao, J., Lanthanide MOFs for Inducing Molecular Chirality of Achiral Stilbazolium with Strong Circularly Polarized Luminescence and Efficient Energy Transfer for Color Tuning. *Chem. Sci.* **2020**, *11*, 9154–9161. (i) Leo, P.; Orcajo, G.; García, J. A.; Ortuño, A. M.; Cuerva, J. M.; Briones, D.; Calleja, G.; Rodríguez-Diéguez, A.; Sanz, R.;

Cepeda, J.; Martínez, F., An Enantiomeric Pair of Alkaline-Earth Metal Based Coordination Polymers Showing Room Temperature Phosphorescence and Circularly Polarized Luminescence. *J. Mater. Chem. C* **2021**, *9*, 5544–5553. (j) Zhao, T.; Han, J.; Shi, Y.; Zhou, J.; Duan, P., Multi-Light-Responsive Upconversion and Downshifting Based Circularly Polarized Luminescent Switches in Chiral Metal–Organic Frameworks. *Adv. Mater.* **2021**, *33*, 2101797. (k) Wang, X.-Z.; Sun, M.-Y.; Huang, Z.; Xie, M.; Huang, R.; Lu, H.; Zhao, Z.; Zhou, X.-P.; Li, D., Turn-on Circularly Polarized Luminescence in Metal–Organic Frameworks. *Adv. Opt. Mater.* **2021**, *9*, 2002096.

(18) (a) Parker, D.; Fradgley, J. D.; Wong, K.-L., The Design of Responsive Luminescent Lanthanide Probes and Sensors. *Chem. Soc. Rev.* **2021**, *50*, 8193–8213. (b) Staszak, K.; Wieszczycka, K.; Marturano, V.; Tylkowski, B., Lanthanides Complexes – Chiral Sensing of Biomolecules. *Coord. Chem. Rev.* **2019**, *397*, 76–90.

(19) Zhang, D.-W.; Li, M.; Chen, C.-F., Recent Advances in Circularly Polarized Electroluminescence Based on Organic Light-Emitting Diodes. *Chem. Soc. Rev.* **2020**, *49*, 1331–1343.

(20) (a) Cerdán, L.; García-Moreno, S.; Costela, A.; García-Moreno, I.; de la Moya, S., Circularly Polarized Laser Emission Induced in Isotropic and Achiral Dye Systems. *Sci. Rep.* **2016**, *6*, 28740. (b) Jiménez, J.; Cerdán, L.; Moreno, F.; Maroto, B. L.; García-Moreno, I.; Lunkley, J. L.; Muller, G.; de la Moya, S., Chiral Organic Dyes Endowed with Circularly Polarized Laser Emission. *J Phys Chem C* **2017**, *121*, 5287–5292. (c) Cerdán, L.; Moreno, F.; Johnson, M.; Muller, G.; de la Moya, S.; García-Moreno, I., Circularly Polarized Laser Emission in Optically Active Organic Dye Solutions. *Phys. Chem. Chem. Phys.* **2017**, *19*, 22088–22093. (d) Dai, W.; Wang, Y.; Li, R.; Fan, Y.; Qu, G.; Wu, Y.; Song, Q.; Han, J.; Xiao, S., Achieving Circularly Polarized Surface Emitting Perovskite Microlasers with All-Dielectric Metasurfaces. *ACS Nano* **2020**, *14*, 17063–17070.

(21) MacKenzie, L. E.; Pal, R., Circularly Polarized Lanthanide Luminescence for Advanced Security Inks. *Nat. Rev. Chem.* **2021**, *5*, 109–124.

(22) Note that we use the following abbreviations for the conjugated carboxylates of the fluorophores, PyC^-, AnC^-, PeC^-, throughout this paper.

(23) (a) Winnik, F. M., Photophysics of Preassociated Pyrenes in Aqueous Polymer Solutions and in Other Organized Media. *Chem. Rev.* **1993**, *93*, 587–614. (b) Ohishi, Y.; Inouye, M., Circularly Polarized Luminescence from Pyrene Excimers. *Tetrahedron Lett.* **2019**, *60*, 151232.

(24) Greenfield, J. L.; Wade, J.; Brandt, J. R.; Shi, X.; Penfold, T. J.; Fuchter, M. J., Pathways to Increase the Dissymmetry in the Interaction of Chiral Light and Chiral Molecules. *Chem. Sci.* **2021**, *12*, 8589–8602.

(25) (a) Kano, K.; Matsumoto, H.; Hashimoto, S.; Sisido, M.; Imanishi, Y., A Chiral Pyrene Excimer in Gamma-Cyclodextrin Cavity. *J. Am. Chem. Soc.* **1985**, *107*, 6117–6118. (b) Kano, K.; Matsumoto, H.; Yoshimura, Y.; Hashimoto, S., Binding Sites of Pyrene and Related Compounds and Chiral Excimer Formation in the Cavities of Cyclodextrins and Branched Cyclodextrins. *J. Am. Chem. Soc.* **1988**, *110*, 204–209. (c) Hayashi, K.; Miyaoka, Y.; Ohishi, Y.; Uchida, T.-a.; Iwamura, M.; Nozaki, K.; Inouye, M., Observation of Circularly Polarized Luminescence of the Excimer from Two Perylene Cores in the Form of [4]Rotaxane. *Chem. Eur. J.* **2018**, *24*, 14613–14616.

(26) As the CD-MOF crystals were isolated from saturated mother liquors, they were rinsed thoroughly to eliminate any residual mother liquors and solutes to ensure that the detected guests are indeed trapped in the CD-MOFs prior to their release by digestion.

(27) Yang, C.; Chen, W.; Zhu, X.; Song, X.; Liu, M., Self-Assembly and Circularly Polarized Luminescence from Achiral Pyrene-Adamantane Conjugates by Selective Inclusion with Cyclodextrins. *J. Phys. Chem. Lett.* **2021**, *12*, 7491–7496.

(28) Dolomanov, O. V.; Bourhis, L. J.; Gilde, R. J.; Howard, J. A. K.; Puschmann, H., *Olex2*: A Complete Structure Solution, Refinement and Analysis Program. *J. Appl. Crystallogr.* **2009**, *42*, 339–341.

(29) Albano, G.; Pescitelli, G.; Di Bari, L., Chiroptical Properties in Thin Films of Π-Conjugated Systems. *Chem. Rev.* **2020**, *120*, 10145–10243.

(30) Sawai, M.; Matsumoto, S.; Mimura, Y.; Imai, Y.; Yamazaki, S.; Kanehisa, N.; Tohnai, N.; Nakata, E.; Takashima, H., Circularly Polarized Luminescence Characteristics of Hydrophobic Pyrene Derivatives/Cyclodextrin Complexes in Aqueous Solution Dissolved by Grinding. *J. Inclusion Phenom. Macrocyclic Chem.* **2022**, *102*, 133–142.

(31) Blok, P. M. L.; Dekkers, H. P. J. M., Measurement of the Circular Polarization of the Luminescence of Photoselected Samples under Artifact-Free Conditions. *Appl. Spectrosc.* **1990**, *44*, 305–309.

(32) Gonzalez-Garcia, M. C.; Salto-Giron, C.; Herrero-Foncubierta, P.; Peña-Ruiz, T.; Giron-Gonzalez, M. D.; Salto-Gonzalez, R.; Perez-Lara, A.; Navarro, A.; Garcia-Fernandez, E.; Orte, A., Dynamic Excimer (Dynex) Imaging of Lipid Droplets. *ACS Sensors* **2021**, *6*, 3632–3639.

(33) Tanaka, H.; Inoue, Y.; Mori, T., Circularly Polarized Luminescence and Circular Dichroisms in Small Organic Molecules: Correlation between Excitation and Emission Dissymmetry Factors. *ChemPhotoChem* **2018**, *2*, 386–402.

Captions for the Figures

Figure 1 | Crystal structure of $AnC^{-}\subset$CD-MOF-1 displaying its color-coded body-centered cubic voids and tunnels viewed along *c* direction (top row) and diagonally (bottom row), displaying (left) and excluding (right) γ-CDs and K^{+} cations for the sake of clarity.

Figure 2 | Graphical illustrations of π-stacked PyC^{-} anionic dimers encapsulated by $(\gamma\text{-CD})_2$ tunnels in CD-HF obtained by solid-state X-ray diffraction of $PyC^{-}\subset$CD-HF viewed: (a) through the opening of the tori, (b) tilted, and (c) normally from the sides, showing the carbon atoms of γ-CD in black and PyC^{-} in green, excluding all the hydrogen atoms and neighboring molecules for the sake of clarity. Stacked partial ^{1}H NMR spectra for the titration of PyC^{-} with γ-CD, and the fitted binding isotherm (d and e).

Figure 3 | Tilted side-on view of $(\gamma\text{-CD})_2$ tunnels in the CD-MOF-1 obtained by solid-state X-ray diffraction of $AnC^{-}\subset$CD-MOF (a) whose structure is drawn in 2D indicating the location and distances of the inward CH-OH groups of α-D-glucopyranosyl residues residing in $(\gamma\text{-CD})_2$ tunnels in the CD-MOF-1 (b). Tilted side-views of $(\gamma\text{-CD})_2$ tunnels in the CD-HF encapsulating PyC^{-} anions obtained by solid-state X-ray diffraction of $PyC^{-}\subset$CD-HF (c–e), and its superstructure drawn in 2D indicating the length and location of the hydrogen bonding interactions established between PyC^{-} anions and γ-CD in the CD-HF (f). Hydrogen atoms, neighboring K^{+} cations, and γ-CD molecules and the other existing π-stacked PyC^{-} anion are omitted for the sake of clarity.

Figure 4 | Solid-state superstructure of $PyC^{-}\subset$CD-HF obtained by X-ray diffraction displaying a spacefill depth cue presentation of the helix-like positioning of the π-stacked PyC^{-} anionic dimers in black held around an enantiomorphous 3_2 screw axis viewed along *c* direction while excluding the CD-HF and every other hydrogen atom for clarity sake (a) helix-like positioning of the π-stacked PyC^{-} anoinic dimers with and without the color-coded presentation of the chiral voids of

the CD-HF viewed along *c* direction (b, top row) and c^* direction (b, bottom row), and extended solid-state superstructure of $PyC^-\subset$CD-HF obtained by X-ray diffraction displaying space-fill PyC^- anionic dimers in yellow and excluding every hydrogen atom for the sake of clarity (c), and comparative X-ray powder diffraction data obtained from the cubic CD-MOF-1 and trigonal CD-HFs.

Figure 5 | Photophysical properties of $PyC^-\subset$CD-HF crystals in the solid-state. (a) Normalized steady-state luminescence spectra of (blue trace) $PyC^-\subset$CD-HF crystals dispersed in $BaSO_4$ (λ_{ex} = 340 nm) in the integrating sphere, (black trace) a single $PyC^-\subset$CD-HF crystal excited with epillumination (λ_{ex} = 340 nm) through a microscope objective, and (red trace) a single $PyC^-\subset$CD-HF crystal illuminated at a specific point (λ_{ex} = 375 nm) via a confocal microscope equipped with a spectrograph analyzer, as shown in panel c. (b) FLIM image of individual $PyC^-\subset$CD-HF crystals and the corresponding (c) emission spectra collected at the marked points in the image (λ_{ex} = 375 nm) and (d) luminescence lifetime distributions extracted from the images.

Figure 6 | Chiroptical and photophysical properties of $PyC^-\subset$CD-HF crystals in MeOH suspension. (a) g_{lum} (black trace) and ΔI (violet) values obtained with a LED excitation source of λ_{ex} = 300 nm. (b) Fluorescence (green trace) and SAEMS spectra (black squares (τ_1 = 42 ns), red dots (τ_2 =12 ns) and blue triangles (τ_3 = 2 ns)) of $PyC^-\subset$CD-HF suspended in MeOH (λ_{ex} = 375 nm), (c) FLIM image of individual $PyC^-\subset$CD-HF crystals in MeOH and the corresponding (d) emission spectra collected at the marked points in the image (λ_{ex} = 375 nm) and (e) luminescence lifetime distributions extracted from the images.

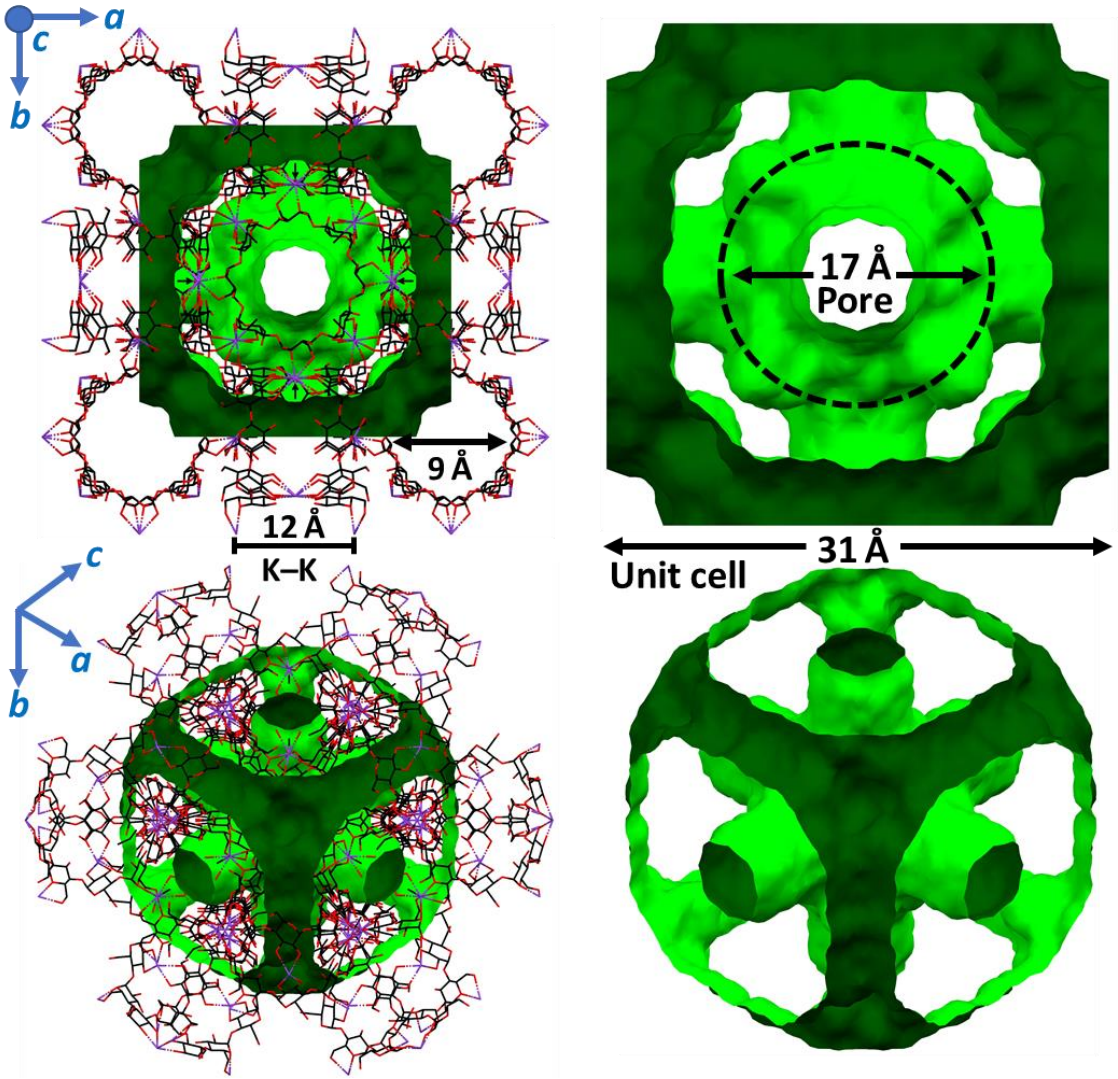

Figure 1

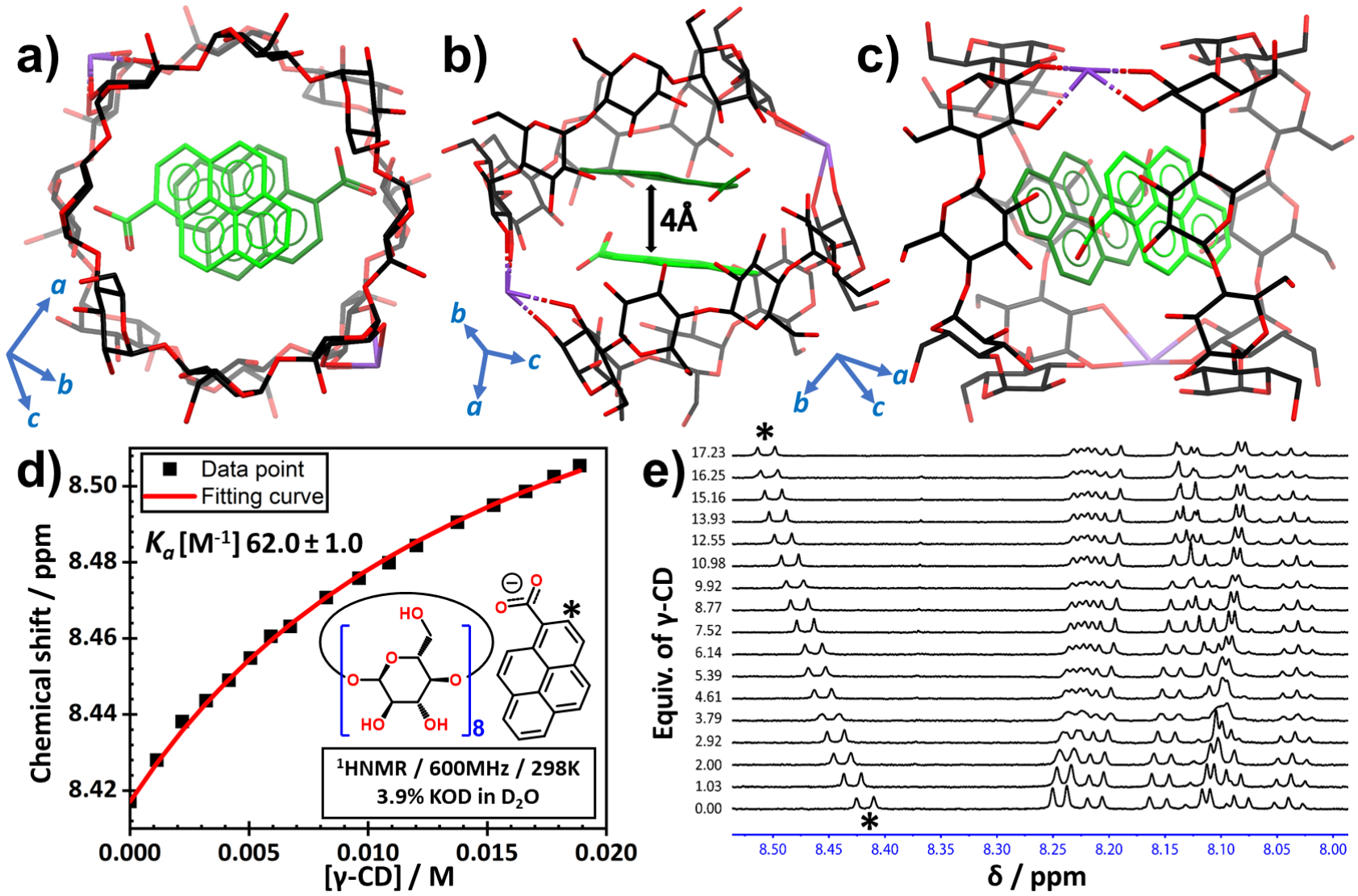
a)
b)
c)
4Å
a
b
c
d)
Data point
Fitting curve
K_a [M^{-1}] 62.0 ± 1.0
Chemical shift / ppm
8.50
8.48
8.46
8.44
8.42
0.000
0.005
0.010
0.015
0.020
[γ-CD] / M
HO
O
OH
8
¹HNMR / 600MHz / 298K
3.9% KOD in D$_2$O
e)
Equiv. of γ-CD
17.23
16.25
15.16
13.93
12.55
10.98
9.92
8.77
7.52
6.14
5.39
4.61
3.79
2.92
2.00
1.03
0.00
8.50
8.45
8.40
8.35
8.30
8.25
8.20
8.15
8.10
8.05
8.00
δ / ppm

Figure 2

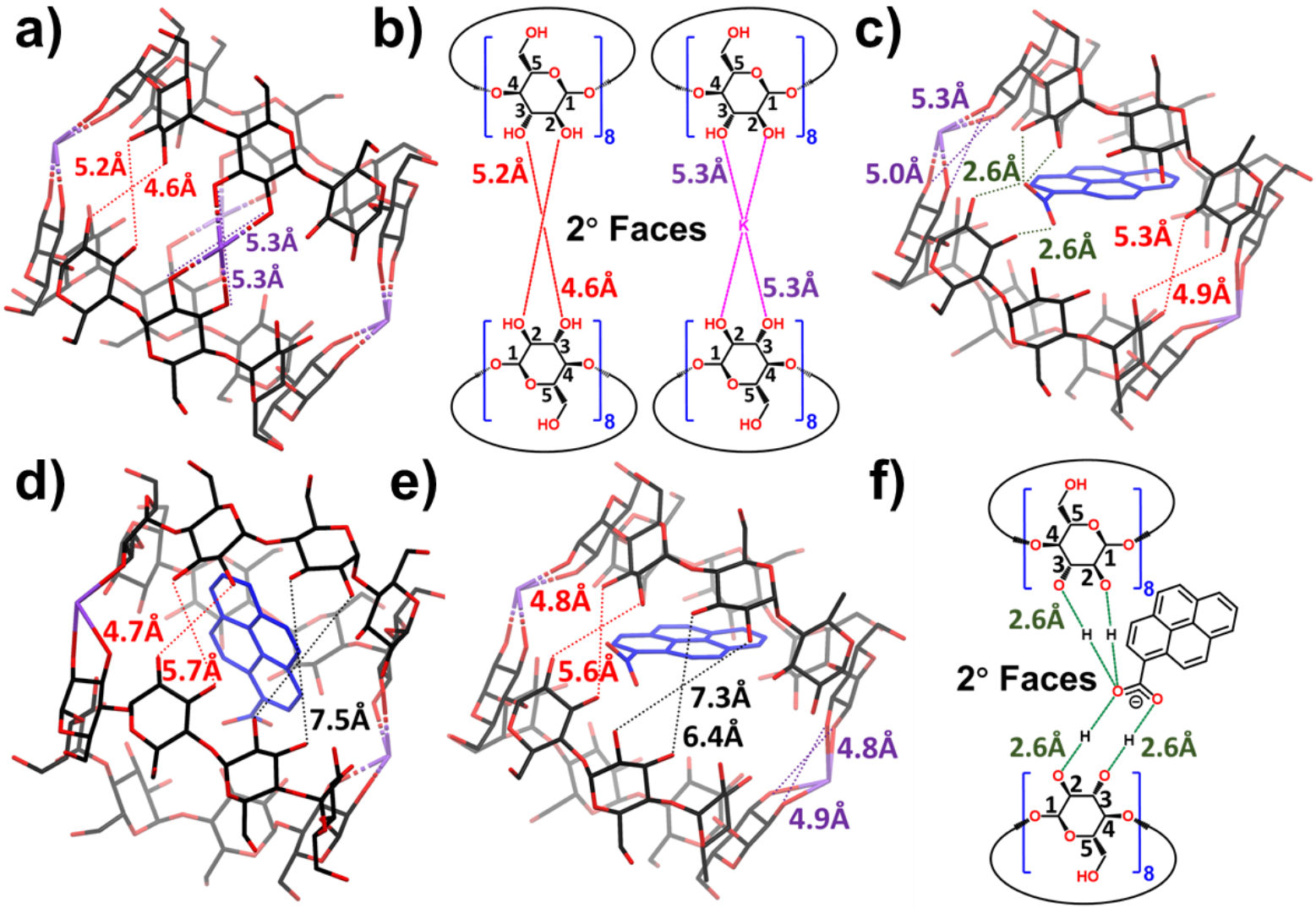
a)
5.2Å
4.6Å
5.3Å
5.3Å
b)
5.2Å
4.6Å
2° Faces
5.3Å
5.3Å
c)
5.3Å
5.0Å
2.6Å
2.6Å
5.3Å
4.9Å
d)
4.7Å
5.7Å
7.5Å
e)
4.8Å
5.6Å
7.3Å
6.4Å
4.8Å
4.9Å
f)
2.6Å
2° Faces
2.6Å
2.6Å

Figure 3

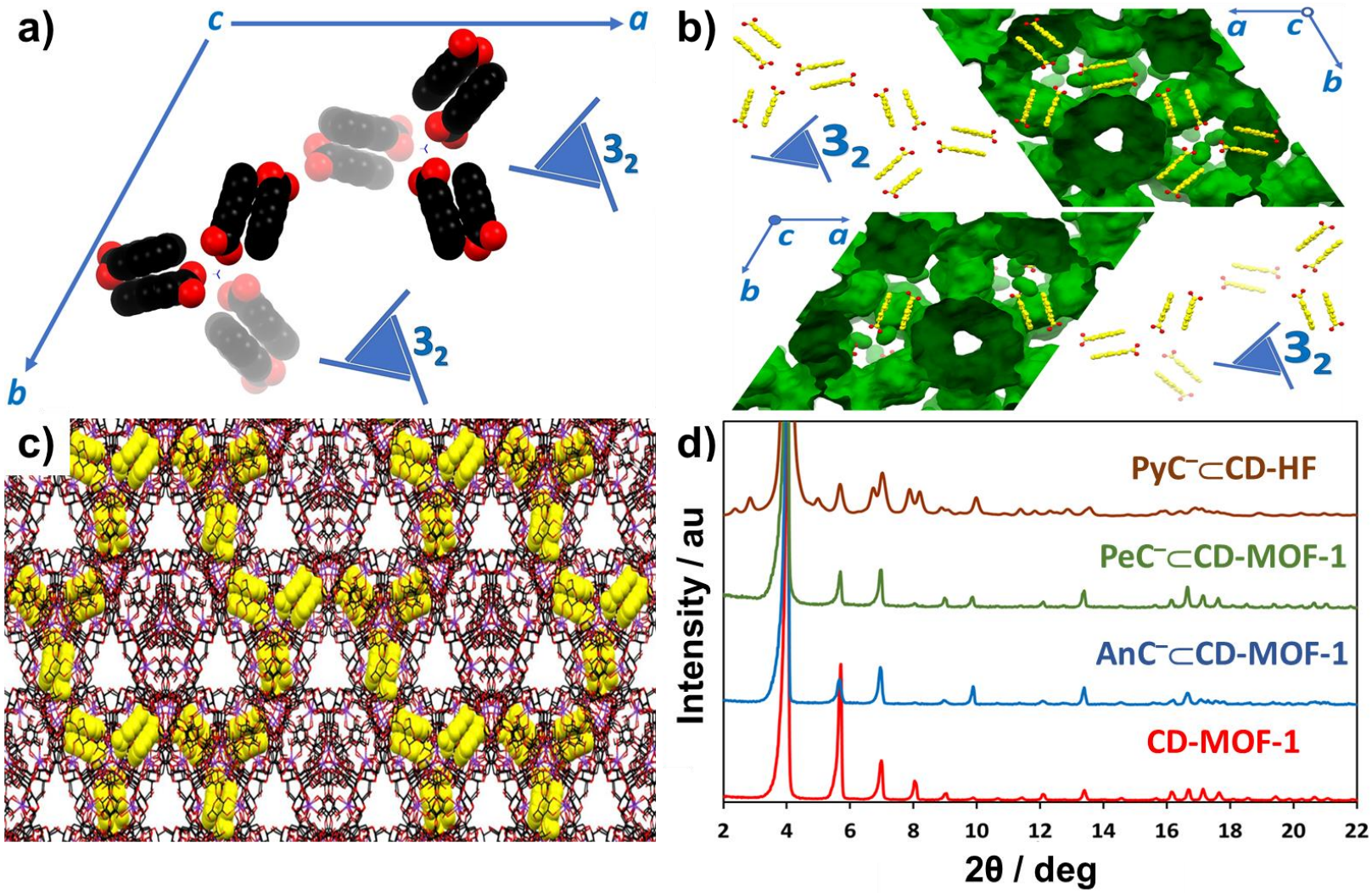
a)
c
a
b
3₂
3₂
b)
a
c
b
3₂
c
a
b
3₂
c)
d)
Intensity / au
PyC⁻⊂CD-HF
PeC⁻⊂CD-MOF-1
AnC⁻⊂CD-MOF-1
CD-MOF-1
2
4
6
8
10
12
14
16
18
20
22
2θ / deg

Figure 4

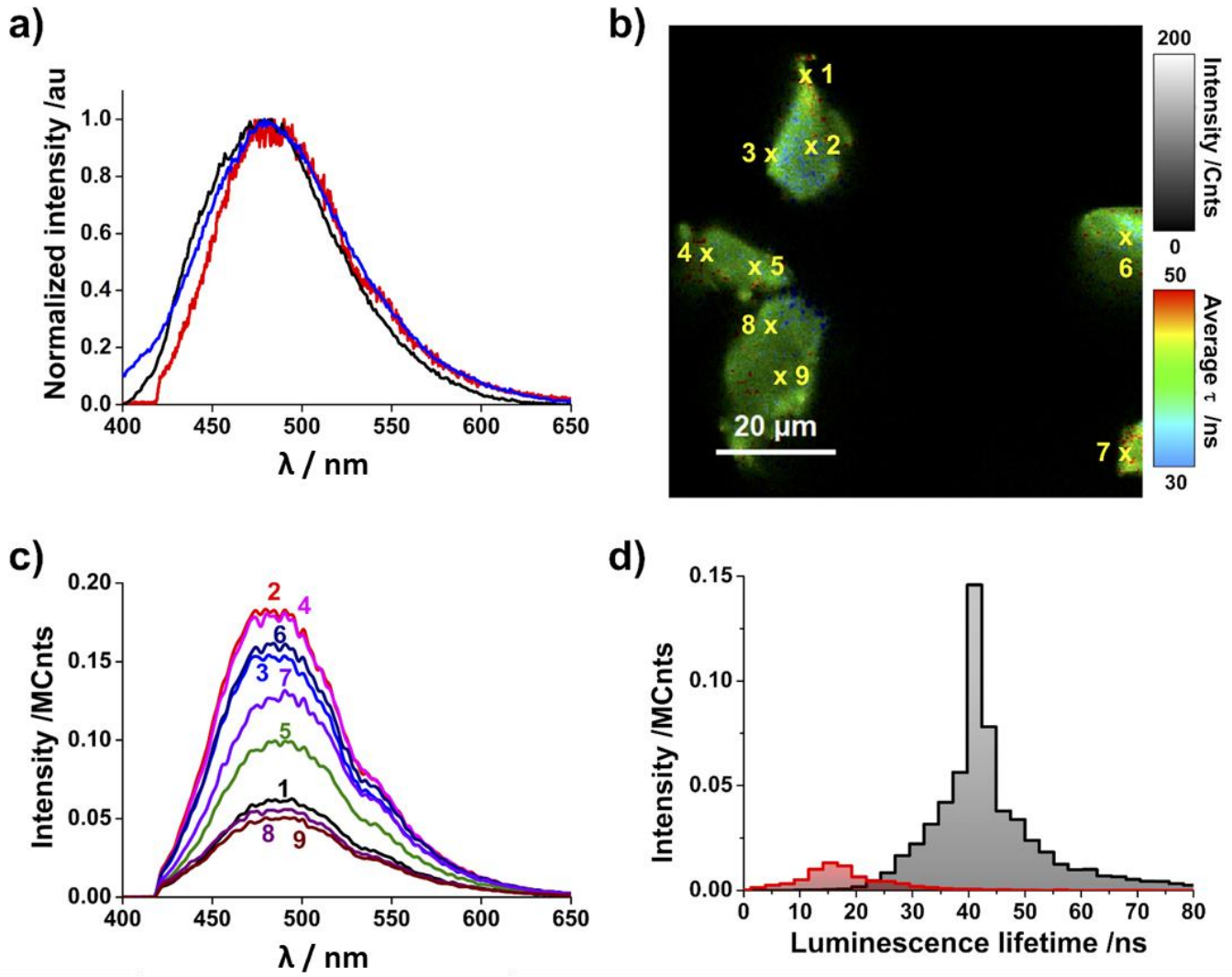
a)
Normalized intensity /au
λ / nm
b)
x 1
3 x
x 2
4 x
x 5
8 x
x 9
x 6
7 x
20 µm
200
Intensity /Cnts
0
50
Average τ /ns
30
c)
Intensity /MCnts
λ / nm
d)
Intensity /MCnts
Luminescence lifetime /ns

Figure 5

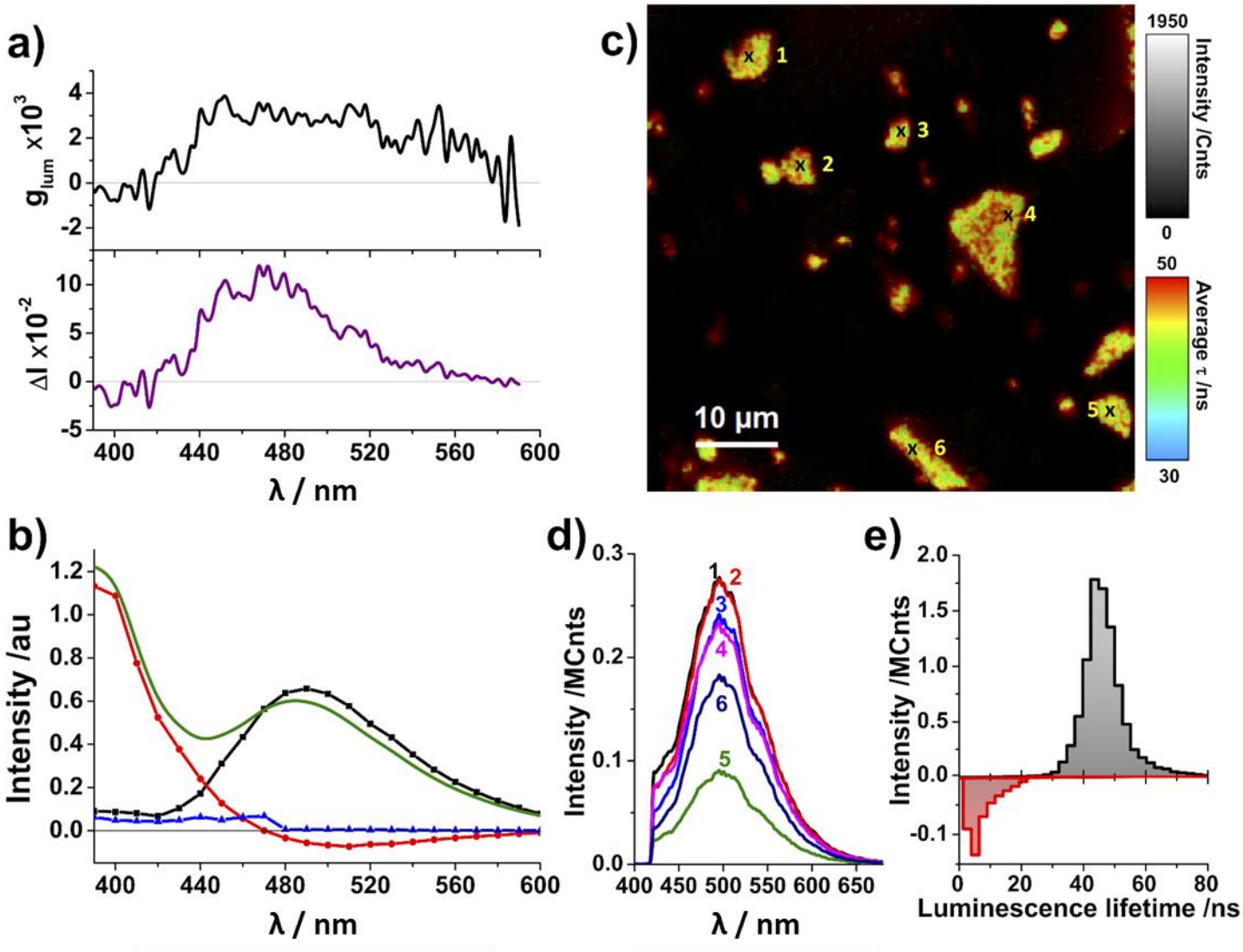
a)
g_{lum} x10^3
4
2
0
-2
ΔI x10^{-2}
10
5
0
-5
400
440
480
520
560
600
λ / nm
b)
Intensity /au
1.2
1.0
0.8
0.6
0.4
0.2
0.0
400
440
480
520
560
600
λ / nm
c)
1
2
3
4
5
6
10 μm
1950
Intensity /Cnts
0
50
Average τ /ns
30
d)
Intensity /MCnts
0.3
0.2
0.1
0.0
1
2
3
4
6
5
400 450 500 550 600 650
λ / nm
e)
Intensity /MCnts
2.0
1.5
1.0
0.5
0.0
-0.1
0
20
40
60
80
Luminescence lifetime /ns

Figure 6

Table of Contents Graphic